Contrib Mineral Petrol (2007) 154:675–689
DOI 10.1007/s00410-007-0216-6

ORIGINAL PAPER

Monazite begets monazite: evidence for dissolution of detrital monazite and reprecipitation of syntectonic monazite during low-grade regional metamorphism

Birger Rasmussen · Janet R. Muhling

Received: 28 December 2006 / Accepted: 3 May 2007 / Published online: 26 May 2007

Abstract Back-scattered electron (BSE) imaging and X-ray element mapping of monazite in low-grade metasedimentary rocks from the Paleoproterozoic Stirling Range Formation, southwestern Australia, reveal the presence of distinct, high-Th cores surrounded by low-Th, inclusion-rich rims. Previous geochronology has shown that the monazite cores are older than 1.9 Ga and overlap with the ages of detrital zircon grains (~3.5–2.0 Ga), consistent with a detrital origin. Many cores have scalloped and embayed surfaces indicating partial dissolution of former detrital grains. Textural evidence links the growth of the monazite rims (~1.2 Ga) to deformation and regional metamorphism during the Mesoproterozoic Albany-Fraser orogeny. These results indicate that high-Th detrital monazite is unstable under low-grade metamorphic conditions (<400°C) and was partially or completely dissolved. Dissolution was followed by near-instantaneous reprecipitation and the formation of low-Th monazite and $ThSiO_4$. This reaction is likely to operate in other low-grade metasedimentary rocks, resulting in the progressive replacement of detrital monazite by metamorphic monazite during regional prograde metamorphism.

Communicated by T.L. Grove.

B. Rasmussen (✉)
School of Earth and Geographical Sciences M006,
The University of Western Australia, 35 Stirling Highway,
Crawley, WA 6009, Australia
e-mail: brasmuss@cyllene.uwa.edu.au

J. R. Muhling
Centre for Microscopy, Characterisation and Analysis M010,
The University of Western Australia, 35 Stirling Highway,
Crawley, WA 6009, Australia

Keywords Monazite · Accessory minerals · Low-grade metamorphism · Geochronology · Rare earth elements · Metamorphic reactions

Introduction

Monazite is a light rare-earth element (REE) phosphate mineral [$(La,Ce,Nd)PO_4$] that incorporates significant amounts of Th and U into its structure. It is a widespread accessory mineral in felsic igneous rocks and amphibolite- and granulite-facies metamorphic rocks, particularly pelitic schists and gneisses (Overstreet 1967; Chang et al. 1996; Spear and Pyle 2002). Monazite is highly suited for geochronology because it excludes common Pb during growth, is resistant to diffusive Pb-loss and is resilient to radiation damage (Seydoux-Guillaume et al. 2002; Cherniak et al. 2004). These properties have led to its growing use in geochronological studies attempting to date magmatic crystallization and to unravel the timing and durations of medium- to high-grade metamorphic episodes, especially in polymetamorphic terranes (DeWolf et al. 1993; Stern and Berman 2000; Catlos et al. 2002; Gibson et al. 2004; Kohn et al. 2005).

Despite advances in the understanding of monazite growth and stability in high-temperature settings, remarkably little is known about the behaviour of monazite during low-temperature processes. This is reflected in the uncertainty regarding the temperature at which new monazite appears in sedimentary rocks, with various studies suggesting that it forms during diagenesis (Donnot et al. 1973; Burnotte et al. 1989; Milodowski and Zalasiewicz 1991; Lev et al. 1998), prehnite–pumpellyite facies metamorphism (Cabella et al. 2001; Rasmussen et al. 2001, 2005), greenschist facies metamorphism (Franz et al. 1996; Wing

et al. 2003) and amphibolite facies metamorphism (Overstreet 1967; Smith and Barriero 1990; Kingsbury et al. 1993; Rubatto et al. 2001).

Similarly, the stability of detrital monazite during prograde metamorphism of sedimentary rocks is poorly documented. An extensive study of the occurrence of monazite worldwide concluded that detrital monazite is unstable and will be destroyed during diagenesis and metamorphism, although no textural evidence was provided (Overstreet 1967). An investigation of the stability of monazite and allanite during prograde metamorphism of pelitic rocks from New England, USA, found cores of detrital monazite surrounded by metamorphic rims in the chlorite zone, while in the biotite zone only metamorphic monazite was observed (Wing et al. 2003). By contrast, an examination of the response of monazite and zircon in Paleozoic turbidites of the Cooma Complex, Australia, to low-pressure greenschist to granulite regional metamorphism found that detrital monazite survived into the amphibolite facies (Williams 2001).

Although monazite has been reported from sub-amphibolite facies metasedimentary rocks, it is not always apparent whether the grains are relict detrital or part of the metamorphic assemblage, and methods for discriminating between these possibilities need to be developed. Clearly, an outstanding problem is knowledge of the reactions causing destruction of detrital monazite. Because monazite is being used increasingly to date geological processes in the upper crust (e.g. very low and low-grade regional metamorphism, hydrothermal mineralization; Rasmussen et al. 2001, 2006a), it is necessary to understand its behaviour in low-temperature settings so that isotopic dates can be correctly interpreted. In this study, we use textural relationships to link monazite growth with low-grade metamorphism of the Stirling Range Formation in southwestern Australia (Fig. 1). We provide textural and geochemical evidence for the partial destruction of detrital monazite and its replacement by metamorphic monazite and $ThSiO_4$. Our results provide insights into the stability of detrital monazite and the possible reactions leading to monazite growth during low-grade metamorphism. We also discuss the implications of our work for U–Th–Pb geochronology of monazite in low- and medium-grade metamorphic rocks.

Geological setting

Albany-Fraser orogen

The Stirling Range Formation is one of a series of low- to medium-grade metasedimentary successions that form part of the Albany-Fraser Orogen in southwestern Australia (Fig. 1). The orogen is exposed on the south and southeast margins of the Yilgarn Craton, and has been interpreted to record continental collision and suturing of the West Australian Craton and the Mawson Craton (comprising the South Australian Craton and parts of Antarctica; Clark et al. 2000). It comprises an autochthonous northern domain containing structurally and thermally reworked mid- to late-Archean granites of the Yilgarn Craton (Beeson et al. 1988; Black et al. 1992); a series of allochthonous complexes, which mostly comprise granulite facies orthogneiss and less abundant paragneiss and metagabbro; late-tectonic granites (Nelson et al. 1995; Clark et al. 1999, 2000; Condie and Myers 1999); and the metasedimentary packages including the Stirling Range Formation and Mount Barren Group (Fig. 1).

In the eastern part of the orogen, two thermotectonic episodes have been identified: the first event (Stage I) occurred between ~1,345 and ~1,260 Ma, and involved high-grade metamorphism, thrusting, transpression and felsic plutonism. It was followed by 45 m.y. of quiescence prior to Stage II, between ~1,215 and ~1,140 Ma, which involved widespread metamorphism (1,215–1,180 Ma) ranging from greenschist to granulite facies (Clark et al. 2000; Bodorkos and Clark 2004), extensive deformation and the intrusion of syn- to post-tectonic granites. In metasedimentary rocks of the Mount Barren Group, and granites and granulite-facies gneisses further to the west, ages overwhelmingly correspond to Stage II (Black et al. 1992; Dawson et al. 2003). Swarms of dolerite dykes, the Gnowangerup and Fraser dyke swarms, intruded the southern and southeastern margins of the Yilgarn Craton at ~1,215 Ma, coincident with Stage II of the Albany-Fraser orogeny (Wingate et al. 2000; Rasmussen and Fletcher 2004).

Stirling Range Formation

The Stirling Range Formation is a succession of low-grade metasedimentary rocks (Muhling and Brakel 1985), exposed in a narrow corridor less than 100 km long and 20 km wide that comprises the Stirling Range (Fig. 1). The rocks are mostly quartzite with minor metamorphosed siltstone and shale, and preserve a variety of sedimentary structures, which indicate that deposition occurred in tide-dominated shallow marine and shelf environments (Cruse et al. 1993; Cruse and Harris 1994; Bengtson et al. 2007). Stratigraphic sections are exposed on many of the peaks in the range; however, correlation between individual peaks has not been possible because of incomplete outcrop, lack of marker beds, and lateral facies changes (Muhling and Brakel 1985). The rocks have undergone folding, faulting and low-grade metamorphism (Boulter 1979; Muhling and Brakel 1985;

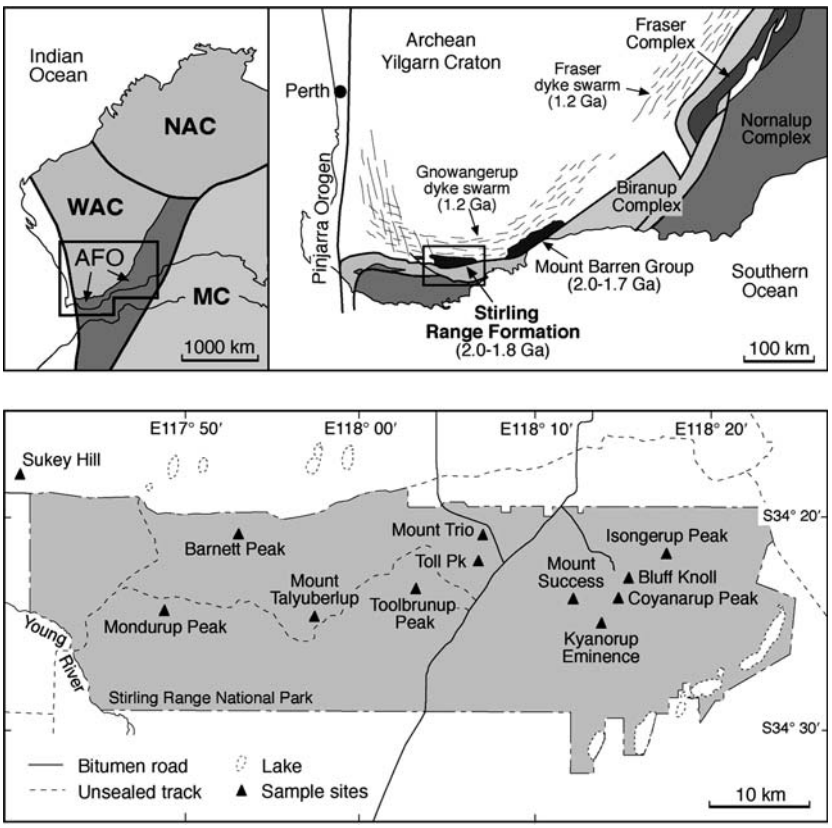

Fig. 1 Regional geology of the Proterozoic Albany-Fraser Orogen (AFO), southwestern Australia and the location of sample sites in the Paleoproterozoic Stirling Range Formation. *WAC* West Australian Craton; *NAC* North Australian Craton; *MC* Mawson Craton

Harris and Beeson 1993). The intensity of folding increases from the north where folds are open and upright, to the south where folds are tight and steeply inclined with axial surfaces that strike broadly northeast–southwest and dip to the south (Beeson 1991; Harris and Beeson 1993). A spaced cleavage is present throughout the succession, but is most strongly developed in the south toward major east-northeast striking basement structures (Harris and Beeson 1993).

The age of the succession is constrained by U–Pb dating of diagenetic xenotime, which indicates a minimum age of ~1.8 Ga (Rasmussen et al. 2004), whereas detrital zircon provides a maximum age of ~2.0 Ga (Rasmussen et al. 2002). Thus, the Stirling Range Formation is between 2.0 and 1.8 billion years old. Uranium–lead dating of metamorphic monazite from the Stirling Range Formation gives an age of ~1.2 Ga (Rasmussen et al. 2002). The timing of monazite growth therefore coincides with peak metamorphism (~1.2 Ga) in nearby greenschist- to amphibolite-facies metasedimentary rocks of the Mount Barren Group (Dawson et al. 2003; Rasmussen et al. 2006b), and is also broadly synchronous with a major granulite-facies tectonothermal event (~1,215–1,140 Ma) in the adjacent Albany-Fraser Orogen (Black et al. 1992). This date also corresponds with the age of several east–west trending dolerite dykes of the Gnowangerup dyke swarm (~1,215 Ma) that intrude the Stirling Range Formation (Rasmussen and Fletcher 2004).

Samples and methods

Samples of metamorphosed sandstone, siltstone and shale of the Stirling Range Formation were collected from 12 peaks in the Stirling Range (Fig. 1). Sixty-four polished thin-sections (PTS) were prepared from these samples, most of which are from Barnett Peak, and samples from two previous studies (Beeson 1991; Cruse 1991). Each polished thin section was examined by optical microscope and a JEOL JSM-6400 scanning electron microscope (SEM) fitted with an Oxford Instruments Link Analytical energy dispersive X-ray spectrometer (EDS).

The sandstones are generally well sorted, and mostly contain detrital quartz, with minor lithic fragments, mica and a range of heavy minerals including zircon, hematite, ilmenite, magnetite, rutile, apatite, monazite, tourmaline and xenotime. Diagenetic quartz overgrowths are present in most samples, along with varying amounts of fine-grained, metamorphic phengitic muscovite (av. Si 3.18/11 O),

chlorite and quartz. Xenotime occurs in trace amounts as diagenetic outgrowths on detrital zircon and, less commonly, as detrital grains. Iron- and titanium-oxides are common as trace phases throughout the sandstone matrix. Hematite crystals aligned with the metamorphic fabric, typically surround detrital hematite and altered ilmenite grains, whereas many tourmaline grains are surrounded by irregular syntaxial overgrowths. Interbedded shales and siltstones have been metamorphosed and mostly comprise fine-grained phengitic muscovite, chlorite and quartz. No quantitative thermobarometry has been attempted for the Stirling Range Formation, however the absence of biotite and occurrence of muscovite are consistent with peak metamorphic temperatures of 300–400°C.

A selection of the largest monazite crystals from the examined samples (all from Barnett Peak) were analysed and mapped by electron microprobe. Electron microprobe analyses were collected using an automated JEOL JSM 6400 SEM, fitted with three wavelength-dispersive crystal spectrometers, located in the Centre for Microscopy, Characterisation and Analysis (CMCA) at the University of Western Australia (UWA). Operating conditions of 20 kV accelerating voltage, 100 nA beam current and a ~1–2 μm spot size were employed. Synthetic phosphates and glasses, and natural minerals were used as standards. Methodology for the analysis of monazite followed that of Williams (1996). Wavelength-dispersive X-ray element maps were collected on the same instrument using the same operating conditions, with pixel sizes of ~0.25 μm and counting times of 50 ms per pixel. Data reduction and image manipulation used software from Moran Scientific.

Results

Monazite occurrence

Monazite was identified in most samples and is particularly abundant in metamorphosed fine-grained sandstone and interbedded siltstone from Barnett Peak (Fig. 1), where it is concentrated in heavy mineral seams (Fig. 2a, b) along with relict detrital zircon, Fe-oxides, Fe–Ti-oxides, rutile, apatite, tourmaline and xenotime. Monazite occurs in the sandstone matrix, and ranges in shape from minute (typically <100 μm) idioblastic crystals through to inclusion-rich, xenoblastic crystals (Fig. 2c–e). In places, monazite has partly overgrown adjacent relict detrital grains indicating that it grew after sediment deposition (Fig. 2b, e).

In some samples, monazite shows a textural relationship with the axial planar cleavage in the sandstone, which developed during folding related to the Albany-Fraser orogeny. For example, monazite at a shale-sandstone contact has developed crystal faces that are parallel to the cleavage direction (Fig. 3a–c), which is defined by aligned fine-grained muscovite and hematite crystals. In metamorphosed shales, monazite is commonly elongate and parallel with the slaty cleavage (Fig. 3d). In some samples, monazite encloses minute hematite laths within the sandstone matrix that are aligned with the tectonic cleavage (Fig. 4).

High-contrast BSE imaging of the monazite reveals that most crystals consist of a rounded to irregular core surrounded by a compositionally distinct rim (Fig. 5a–i). Examination of the monazite crystals using polarised light shows that the core and rim in each grain are optically continuous. Unlike the cores, the rims contain numerous fine inclusions (typically 1–2 μm) of predominantly hematite, as well as minor quartz, muscovite, chlorite and Ti-oxide. The minerals enclosed by the monazite rims are identical to those that occur in the metamorphic matrix of the host rocks.

Most cores appear to be compositionally homogeneous in BSE images; however, some display zoning that is truncated at the boundary with the outer rim (Figs. 5a, 6a), and is interpreted to be magmatic in origin. The cores are clearly visible in high-contrast BSE images, delineated by a ''bright'' inner rim zone (typically <5 μm) of monazite (Figs. 5a–i, 6a–c), which in places, contains minute specks of a Th-rich silicate mineral (Fig. 6d). The rims completely enclose most cores and typically form more than 50% of the entire crystal. Within a single sample, monazite cores range in shape from broadly oval to highly irregular with scalloped and embayed outlines (Fig. 6). A detailed examination of the margins of some of the more complete and unaltered cores shows that the core-rim boundary is not entirely smooth, but in places is irregular with serrated outlines (Fig. 6a).

Monazite chemistry

Electron microprobe analyses and X-ray element maps for Ca, Th, La, Sm and Y of monazite grains reveal several distinct compositional differences between the cores and rims (Figs 7, 8, 9, 10, 11). The cores have higher concentrations of Th, U, Pb, Y and Ca, and lower concentrations of Eu and Fe, than the rims (Table 1). Concentrations of ThO_2 and UO_2 for the cores are 5–6 and 0.2–0.3%, respectively, and are typical of high-temperature igneous and metamorphic monazite. By comparison, the rims have <2% ThO_2 and 0–0.1% UO_2, which is characteristic of low-temperature metamorphic and hydrothermal monazite. Calcium is incorporated into monazite by the brabantite substitution, $Ca^{2+} + Th^{4+} = 2REE^{3+}$, and there is a strong correlation between Ca and Th in both the cores and the rims of the

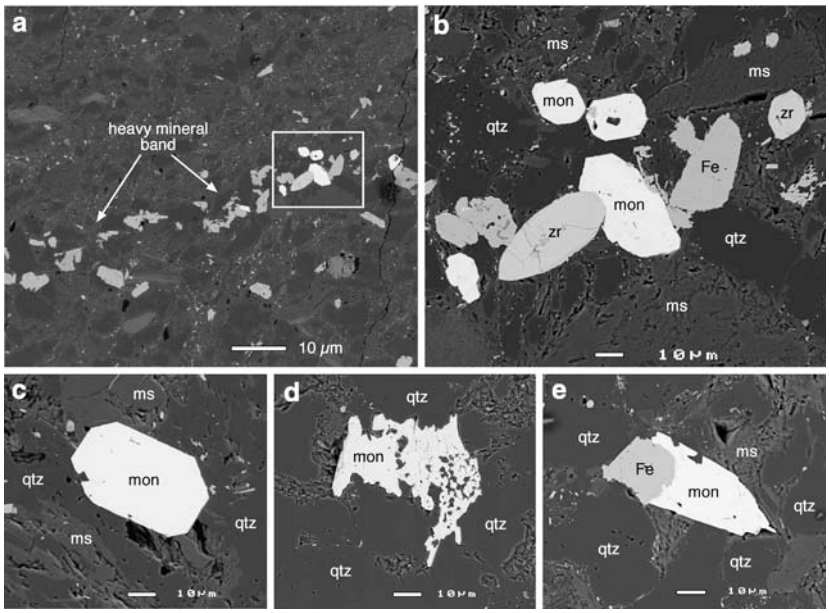

Fig. 2 Back-scattered electron (*BSE*) photomicrographs of monazite (*mon*) in a heavy mineral band within a fine-grained quartz sandstone. The heavy mineral band also comprises Fe-oxides, rutile, apatite, tourmaline and zircon. **b** Closeup of monazite in Fig. 2a (*white rectangular outline*) showing idioblastic monazite crystals (*mon*) and adjacent Fe-oxides (*Fe*) and detrital zircon (*zr*). Barnett Peak, UWA 114324. **c** Idioblastic monazite crystal (*mon*) in a matrix of quartz (*qtz*) and fine-grained muscovite (*ms*). Barnett Peak, UWA 114321. **d** Coarse, xenoblastic monazite crystal with abundant mineral inclusion. Barnett Peak, UWA 114338. **e** An irregular monazite crystal (*mon*) with several planar faces partly enclosing an adjacent grain of Fe-oxide (*Fe*). Barnett Peak, UWA 114325

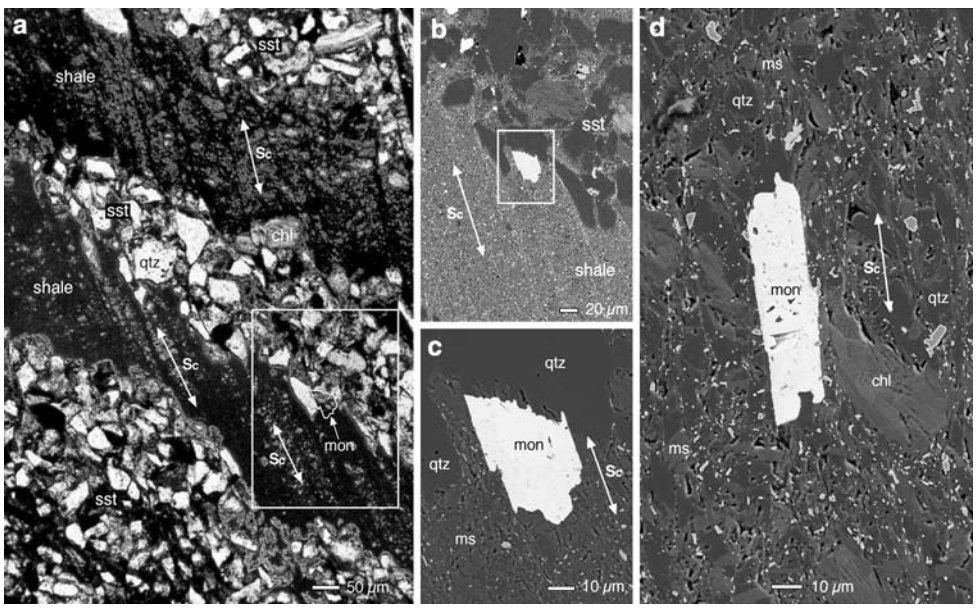

Fig. 3 **a** Interbedded fine-grained sandstone (*sst*) and shale from Barnett Peak; note the development of spaced cleavage (*Sc*) in the shale horizons. Transmitted light optical photograph. **b** BSE photomicrograph of monazite in **a** located at the shale-sandstone contact (*see arrow*). **c** Higher magnification photo of inset in **b** showing the alignment of the two main monazite crystal faces with the orientation of the spaced cleavage (*Sc*). **d** BSE image of an elongate monazite crystal that is oriented parallel with cleavage (*Sc*) defined by aligned fine-grained muscovite (*ms*), Fe-oxides (*light grey*) and quartz crystals. Barnett Peak, UWA 114325

monazite crystals. A characteristic feature of low-temperature monazite is its high Eu_2O_3 content (~0.5%), and this is seen in the rims of the grains from the Stirling Range Formation (0.17–0.94% Eu_2O_3). The concentrations of Eu_2O_3 are very low (<0.06%) in the cores, which is typical of monazite formed at higher temperatures (Fig. 10). The concentrations of FeO are also higher in the rims (0.1–0.3%) than the cores (0.1%), although this could be due in part to the presence of very fine hematite inclusions in the rims.

The cores have mostly uniform compositions, although there are minor variations in the Y_2O_3, ThO_2 and CaO contents that match the magmatic zoning seen in BSE images. By contrast, the rims show a characteristic pattern of strong compositional zoning. The part of the rim closest to the core

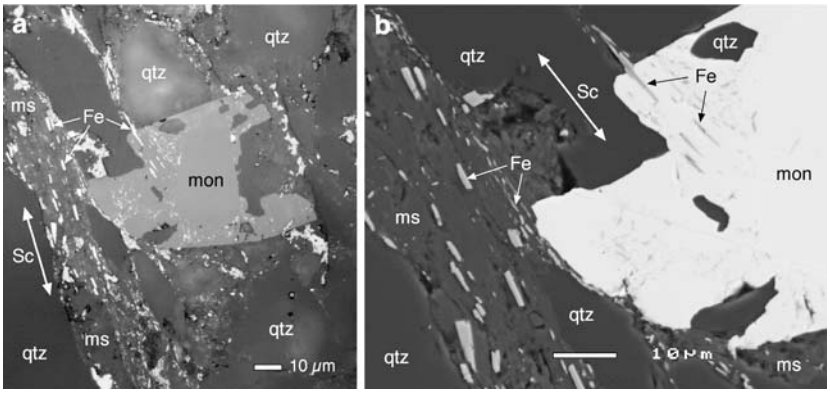

Fig. 4 **a** Large monazite crystal (*mon*) in the matrix of a quartz sandstone. The monazite (*mon*) has engulfed metamorphic Fe-oxide laths in the fine-grained muscovite (*ms*) matrix, which are parallel with the cleavage direction. Reflected light photomicrograph. **b** BSE image of **a** showing Fe-oxide laths (*Fe*) in the fine-grained muscovite (*ms*) matrix and as inclusions within monazite (*mon*). Barnett Peak, UWA 114325

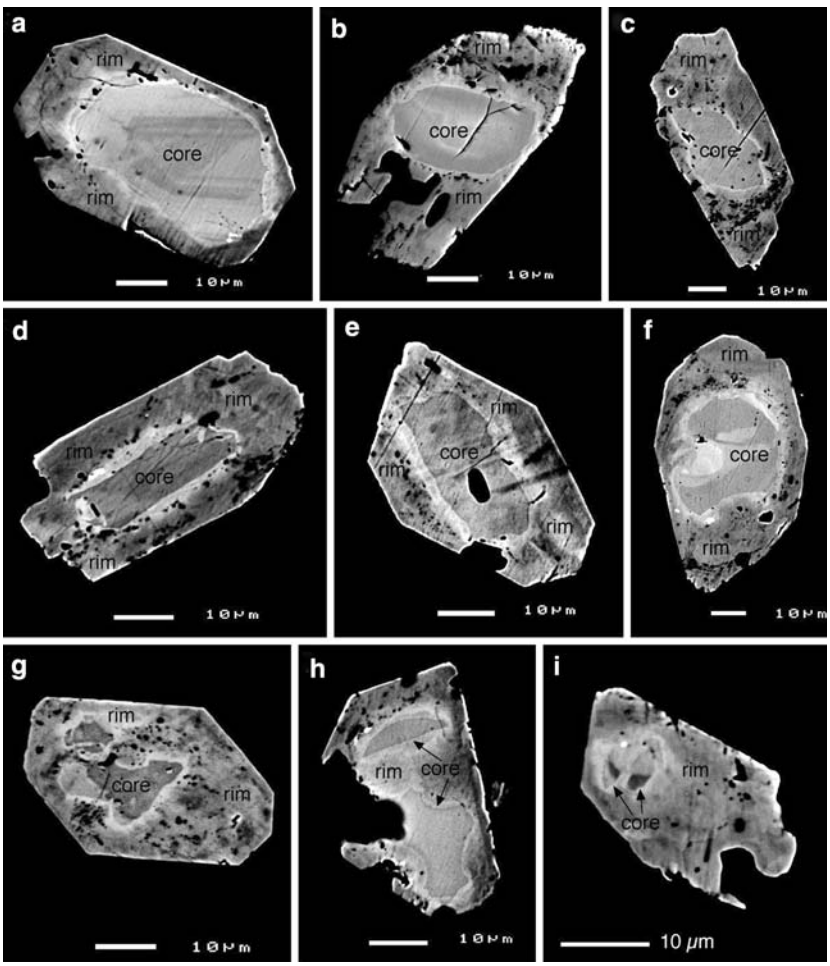

Fig. 5 High-contrast BSE images of monazite with a compositionally distinct core surrounded by an inclusion-rich rim defining idioblastic to subidioblastic crystal outlines. The sequence of images from **a** to **i** show increasing degrees of dissolution, ranging from near-complete cores in **a** through to irregular, embayed remnants in **i**. *Arrows* point to the core-rim contact. All samples are from Barnett Peak. **a** (UWA 114321); **b–d**, **g** (UWA 114324); **e**, **f**, **h** (UWA 114325); **i** (UWA 114321)

has low concentrations of La that are offset by higher amounts of Pr, Nd, Sm, Eu and Gd (~5% La_2O_3; ~24% Nd_2O_3) (Figs. 7e–i, 8c–l). The La-poor zone is about 5 μm wide, and is followed outward by a broader zone in which La concentrations are higher but Nd, Sm, Eu and Gd are all lower (~15% La_2O_3; ~12% Nd_2O_3) (Figs. 7, 8, 10).

The chondrite-normalized REE patterns of the cores and rims are also distinctly different (Fig. 11). The cores

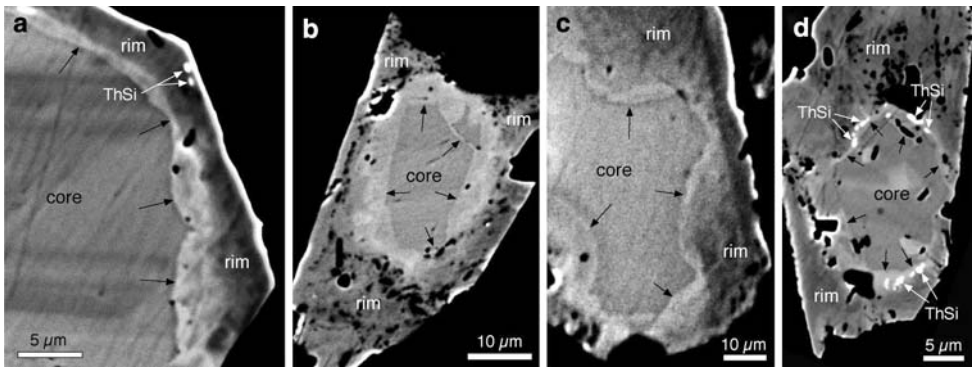

Fig. 6 **a** Close-up of core-rim region showing a compositionally zoned core truncated by an irregular rim forming an idioblastic overgrowth. **b** Detail of an angular core surrounded by an inclusion-rich rim. Barnett Peak, UWA 114325. **c** Close-up of core (Fig. 5h) showing scalloped, embayed margins (*see arrows*). **d** A monazite core lined by numerous minute inclusions of a Th–silicate mineral (*white*). Barnett Peak, UWA 114321

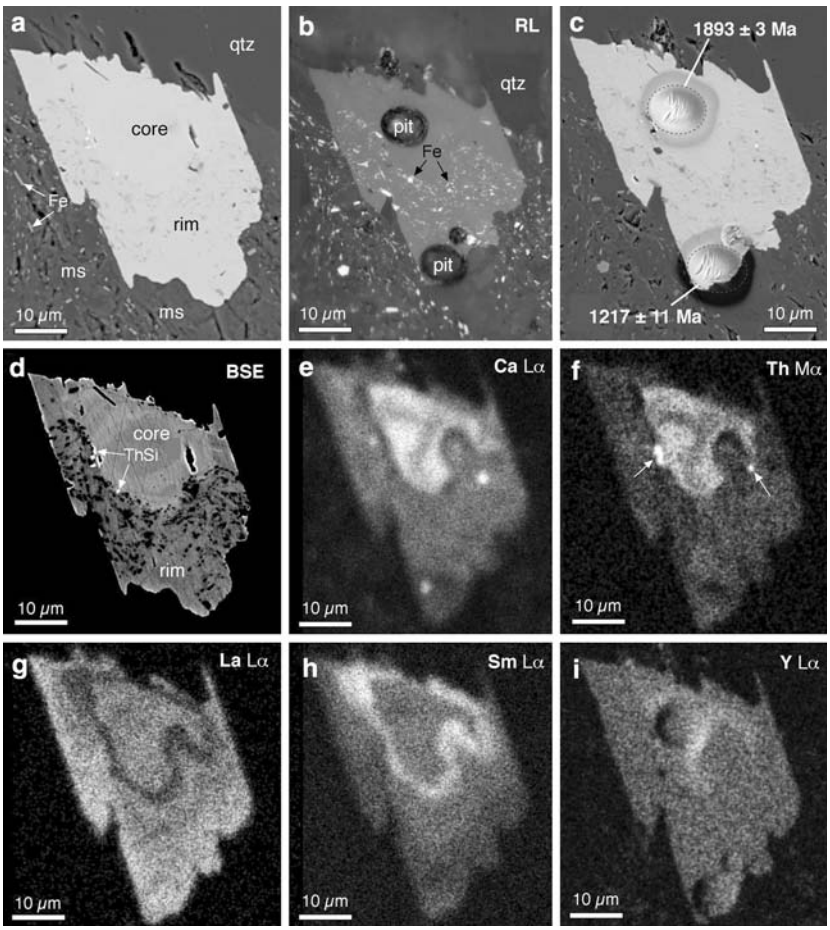

Fig. 7 **a** BSE image of monazite in Fig. 3a–c. **b** Reflected light image of monazite in **a** showing numerous minute Fe-oxide inclusions (*white*) in the fine-grained muscovite (*ms*) matrix and in the monazite rim. **c** BSE image of monazite with two SHRIMP analytical pits and their corresponding ages (1σ precision). Monazite core is a $^{207}Pb/^{206}Pb$ date whereas monazite overgrowth is a $^{208}Pb/^{232}Th$ date. **d** High-contrast BSE image of monazite revealing an irregular core with an inclusion-rich rim. **e** Wavelength dispersive spectrometry (WDS) X-ray maps for Ca, **f** for Th, **g** for La, **h** for Sm, and **i** for Y; note the inverse relationship between La content and Sm content. Note that monazite in **a** and **d** was imaged prior to SHRIMP analysis and repolishing of the mount. Barnett Peak, UWA 114325

have uniform patterns showing a slight enrichment in the LREE and a pronounced negative Eu anomaly. The rims show two REE patterns corresponding to the La-poor and La-rich zones. The La-poor zones have a convex-upward pattern for elements between La and Dy, while the La-rich zones show slight enrichment in LREE from La to Nd, and relatively depleted values for the elements from Sm to Dy. In comparison with the cores, the rims have higher contents of the REE between Pr and Eu, but lower amounts of Tb and Dy, and they have no Eu

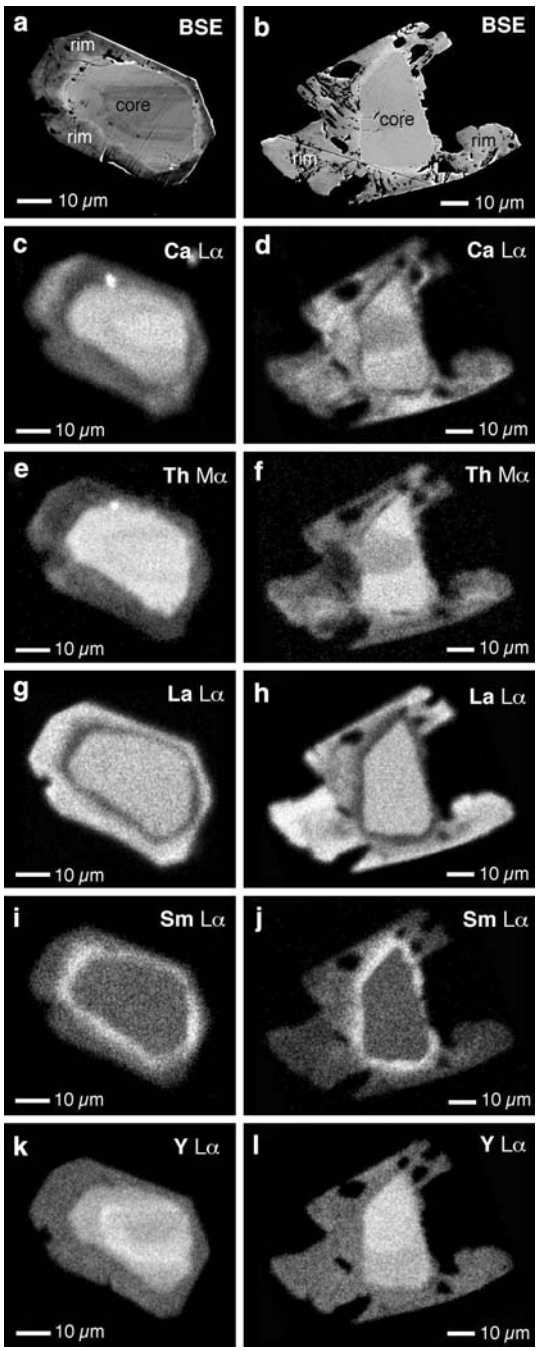

Fig. 8 High-contrast BSE images (**a**, **b**), and WDS X-ray maps for two monazite crystals showing element distribution maps for Ca (**c**, **d**), Th (**e**, **f**), La (**g**, **h**), Sm (**i**, **j**) and Y (**k**, **l**). Note the similarity of distribution patterns for La, Sm and Y in the metamorphic rims. **a**, **c**, **e**, **g**, **i**, **k** (Barnett Peak, UWA 114321); **b**, **d**, **f**, **h**, **j**, **l** (Barnett Peak, UWA 114325)

anomaly (Fig. 11). Cerium contents show little variability, and the rims do not exhibit a Ce anomaly.

Many of the rims contain minute specks (<1 μm) with high Th contents. Qualitative analysis of the Th-rich inclusions by EDS indicates that they also contain Si, suggesting that the mineral may be huttonite or possibly

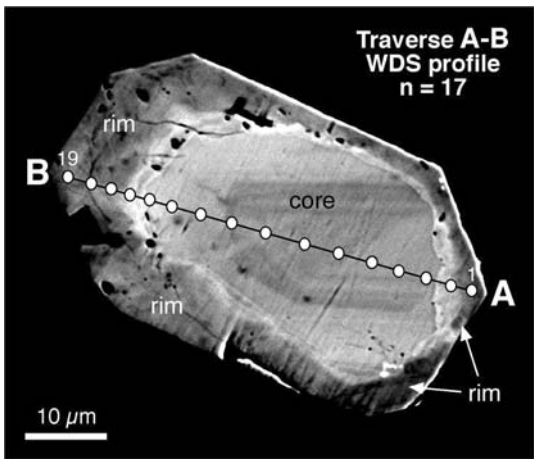

Fig. 9 BSE image of monazite (see Fig. 8a) with a distinct core surrounded by an idiomorphic rim showing the location of electron microprobe traverse *A–B* (see Fig. 10 for element profiles). Barnett Peak, UWA 114321

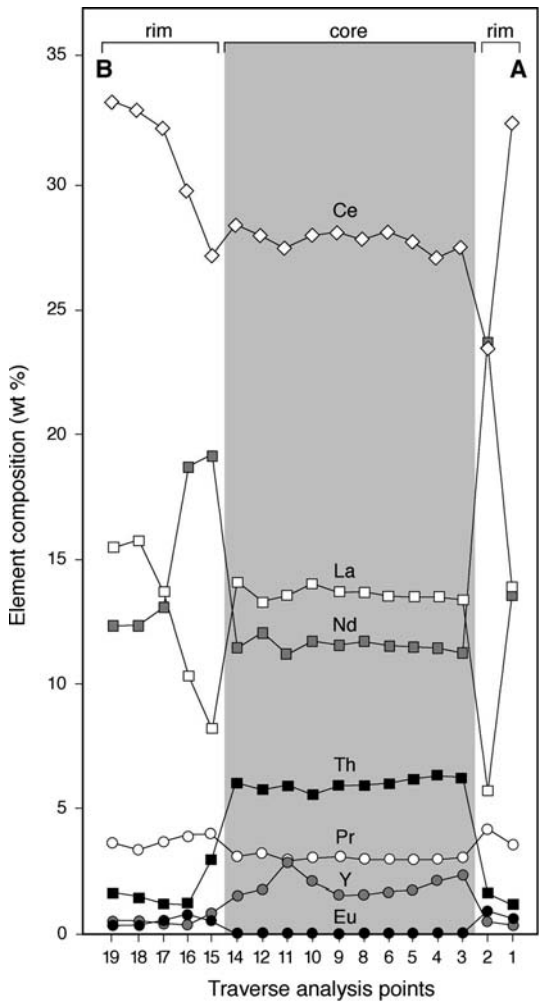

Fig. 10 Electron microprobe traverse (*A–B*) across monazite in Fig. 9 showing variations in La, Ce, Nd, Th, Pr, Y and Eu contents

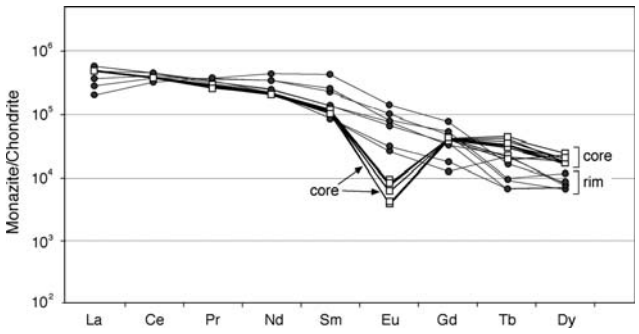

Fig. 11 Chondrite-normalized REE distribution patterns of the monazite core and rim (Figs. 9, 10; Table 1) using chondrite data from McDonough and Sun (1995). Heavy REE are not shown due to their low concentrations (at or below detection limits)

thorite. Some monazite grains have patches of slightly elevated Th around their edges.

Discussion

Monazite replacement during low-grade regional metamorphism

Dissolution of detrital monazite

The concentration of monazite in heavy mineral seams suggests that it was originally introduced into the sedimentary rocks as detritus. The ages of the cores vary between ~2.26 and ~1.9 Ga (Figs. 12, 13) and overlap with the ages of detrital zircon grains from the same locality (~3.5–2.0 Ga; Fig. 13) (Rasmussen et al. 2002). This confirms that the monazite cores are remnants of detrital grains. The composition of the monazite cores (e.g. high Th and U, negative Eu anomaly) is consistent with a high-temperature igneous or metamorphic source for the detrital grains. The truncation of primary compositional zoning in the cores is unlikely to have been caused by element diffusion because this process is considered to be ineffective at such low temperatures (<400°C) (Cherniak et al. 2004; Gardés et al. 2006). Instead, the irregular, scalloped core-rim contact (Fig. 6a) provides strong textural evidence for the partial dissolution of former detrital monazite grains by post-depositional fluids, consistent with experimental results (e.g. Teufel and Heinrich 1997; Seydoux-Guillaume et al. 2002). The incorporation of thorium silicate crystals within rims of metamorphic monazite around the detrital cores suggests that the dissolution of the cores was closely linked in time to the growth of the metamorphic rims.

Formation of metamorphic monazite

There are several lines of evidence indicating that the monazite rims formed during deformation and metamorphism: (1) monazite crystals are commonly idiomorphic, precluding a detrital origin involving abrasion and rounding during sediment transportation and reworking. (2) The rims enclose mineral inclusions, which are identical to metamorphic minerals in the matrix of the host-rocks. (3) Some monazite rims are aligned with the deformational cleavage and enclose elongate grains that are parallel with the rock fabric, which developed during regional metamorphism. (4) The isotopic age of the rims (~1.2 Ga; Figs. 12, 13) corresponds with the age of metamorphism in schists in the nearby Mount Barren Group (~1.2 Ga; Dawson et al. 2003; Rasmussen et al. 2006b) and with the timing of deformation, high-grade metamorphism and granite magmatism in the Albany-Fraser Orogen (~1.2–1.14 Ga; Black et al. 1992; Clark et al. 2000).

Monazite growth in the Stirling Range Formation was synchronous with regional peak metamorphism, which caused pervasive growth of fine-grained muscovite and chlorite. This assemblage is present throughout the succession and indicates that metamorphic temperatures did not exceed ~400°C. There is no textural evidence to suggest that other P- or REE-bearing minerals (e.g. apatite, xenotime, zircon) participated in the formation of metamorphic monazite. Rather, a scenario is envisaged whereby detrital high-temperature monazite grains became unstable during peak greenschist facies metamorphism and were partially or completely dissolved. Shortly afterwards, new metamorphic monazite was precipitated on the relict detrital cores. The overgrowths preferentially grew parallel to the fabric of the metamorphic matrix, engulfing and dissolving particles of muscovite, chlorite and quartz, whereas Fe-oxide particles were largely preserved as inclusions. The dissolution and replacement were not isochemical: some elements (e.g. Eu and Fe) were added while others (e.g. Ca and perhaps Th and Y) were removed. The differences in composition between the detrital monazite cores and the metamorphic monazite rims, particularly the low ThO_2 contents of the latter, probably reflect the different *P–T* conditions and chemical environment under which the new monazite formed. The presence of minute Th-rich inclusions in the metamorphic monazite rims suggests that Th released by dissolution of detrital monazite was immobile, and could not all be accommodated in the metamorphic monazite rims. Their occurrence in the rims suggests that dissolution of the detrital monazite was closely linked in time with precipitation of the metamorphic rims. The preservation of detrital monazite cores in the composite crystals suggests that the conditions (e.g. temperature, fluid composition, flow rate) required for complete replacement of all of the detrital cores were not sustained over a sufficiently long period of time.

X-ray mapping and WDS analysis show that the earliest formed metamorphic monazite contains significantly less

Table 1 Electron microprobe analysis of detrital monazite core and metamorphic rim (see Fig. 10). b.d. Below detection limits

Oxide	1 (A) rim	2 rim	3 core	4 core	5 core	6 core	8 core	9 core	10 core	11 core	12 core	14 core	15 rim	16 rim	17 rim	18 rim	19(B) rim
SiO_2	0.73	0.27	0.41	0.43	0.37	0.38	0.37	0.37	0.41	0.56	0.56	0.55	0.31	0.14	0.52	0.26	0.38
P_2O_5	29.61	30.13	30.40	30.78	30.33	29.98	30.40	31.26	30.77	30.48	29.93	30.32	29.97	30.25	30.00	29.95	30.22
La_2O_3	13.85	5.68	13.37	13.52	13.47	13.55	13.66	13.69	14.03	13.57	13.29	14.16	8.11	10.27	13.72	15.77	15.53
Ce_2O_3	32.60	23.59	27.53	26.98	27.84	28.08	27.90	28.12	27.95	27.54	28.03	28.44	27.11	29.73	32.32	32.99	33.39
Pr_2O_3	3.60	4.13	3.00	3.01	3.03	3.01	3.11	3.13	3.11	2.91	3.22	3.15	4.00	3.96	3.71	3.36	3.63
Nd_2O_3	13.59	23.70	11.23	11.43	11.42	11.46	11.76	11.54	11.69	11.18	12.05	11.49	19.12	18.67	13.11	12.32	12.32
Sm_2O_3	2.38	7.58	2.06	1.89	1.90	1.80	1.87	1.86	1.90	1.86	2.09	1.84	4.53	4.02	2.42	1.53	1.49
Eu_2O_3	0.44	0.94	b.d.	b.d.	0.06	0.05	0.04	b.d.	0.04	b.d.	b.d.	b.d.	0.53	0.68	0.50	0.20	0.17
Gd_2O_3	0.82	1.80	1.04	1.00	0.91	0.93	0.95	0.89	0.88	0.97	0.98	0.92	1.25	1.10	0.75	0.41	0.29
Tb_2O_3	b.d.	0.07	0.08	0.13	0.18	0.09	0.14	0.14	0.13	0.19	0.16	0.12	0.04	0.04	0.10	b.d.	0.09
Dy_2O_3	0.20	0.24	0.66	0.62	0.49	0.52	0.45	0.49	0.58	0.69	0.57	0.50	0.35	0.19	0.20	0.20	0.22
Y_2O_3	0.35	0.42	2.34	2.15	1.77	1.61	1.51	1.58	2.07	2.83	1.71	1.54	0.81	0.36	0.42	0.41	0.44
CaO	0.68	0.37	1.39	1.43	1.37	1.33	1.32	1.35	1.22	1.22	1.07	1.23	0.42	0.58	0.60	0.73	0.54
FeO	0.15	0.14	0.09	0.09	0.08	0.09	0.06	0.08	0.08	0.11	0.10	0.11	0.12	0.14	0.22	0.25	0.27
PbO	0.05	0.17	0.81	0.78	0.73	0.74	0.75	0.74	0.80	0.75	0.67	0.82	0.37	0.05	b.d.	0.08	0.16
ThO_2	1.10	1.58	6.27	6.35	6.21	6.01	5.92	5.89	5.52	5.92	5.72	6.11	2.95	0.95	1.16	1.40	1.64
UO_2	0.05	0.12	0.29	0.34	0.21	0.29	0.22	0.27	0.26	0.29	0.25	0.28	0.13	b.d.	b.d.	0.05	0.14
Total	100.21	100.93	100.96	100.93	100.36	99.91	100.44	101.41	101.42	101.07	100.38	101.57	100.15	101.19	100.07	100.00	100.95
Si	0.028	0.011	0.016	0.016	0.014	0.015	0.014	0.014	0.016	0.021	0.022	0.021	0.012	0.005	0.020	0.010	0.015
P	0.977	0.995	0.991	0.997	0.994	0.991	0.996	1.005	0.996	0.989	0.986	0.987	0.995	0.993	0.986	0.990	0.989
La	0.199	0.082	0.190	0.191	0.192	0.195	0.195	0.192	0.198	0.192	0.191	0.201	0.117	0.147	0.196	0.227	0.222
Ce	0.465	0.337	0.388	0.378	0.395	0.401	0.395	0.391	0.391	0.386	0.399	0.400	0.389	0.422	0.459	0.471	0.473
Pr	0.051	0.059	0.042	0.042	0.043	0.043	0.044	0.043	0.043	0.041	0.046	0.044	0.057	0.056	0.053	0.048	0.051
Nd	0.189	0.330	0.154	0.156	0.158	0.160	0.163	0.157	0.159	0.153	0.167	0.158	0.268	0.259	0.182	0.172	0.170
Sm	0.032	0.102	0.027	0.025	0.025	0.024	0.025	0.024	0.025	0.025	0.028	0.024	0.061	0.054	0.032	0.021	0.020
Eu	0.006	0.012	–	–	0.001	0.001	0.001	–	0.001	–	–	–	0.007	0.009	0.007	0.003	0.002
Gd	0.011	0.023	0.013	0.013	0.012	0.012	0.012	0.011	0.011	0.012	0.013	0.012	0.016	0.014	0.010	0.005	0.004
Tb	–	0.001	0.001	0.002	0.002	0.001	0.002	0.002	0.002	0.002	0.002	0.002	0.001	–	0.001	–	0.001
Dy	0.003	0.003	0.008	0.008	0.006	0.006	0.006	0.006	0.007	0.009	0.007	0.006	0.004	0.002	0.003	0.003	0.003
Y	0.007	0.009	0.048	0.044	0.036	0.033	0.031	0.032	0.042	0.058	0.035	0.032	0.017	0.007	0.009	0.008	0.009
Ca	0.028	0.015	0.057	0.059	0.057	0.056	0.055	0.055	0.050	0.050	0.045	0.051	0.018	0.024	0.025	0.031	0.022
Fe	0.005	0.004	0.003	0.003	0.002	0.003	0.002	0.003	0.003	0.004	0.003	0.003	0.004	0.005	0.007	0.008	0.009
Pb	0.001	0.002	0.008	0.008	0.008	0.008	0.008	0.008	0.008	0.008	0.007	0.008	0.004	–	–	0.001	0.002
Th	0.010	0.014	0.055	0.055	0.055	0.053	0.052	0.051	0.048	0.052	0.051	0.053	0.026	0.008	0.010	0.012	0.014
U	–	0.001	0.002	0.003	0.002	0.003	0.002	0.002	0.002	0.002	0.002	0.002	0.001	–	–	–	0.001
Total	2.013	2.002	2.005	2.000	2.002	2.005	2.001	1.996	2.001	2.003	2.003	2.004	1.998	2.009	2.008	2.012	2.008

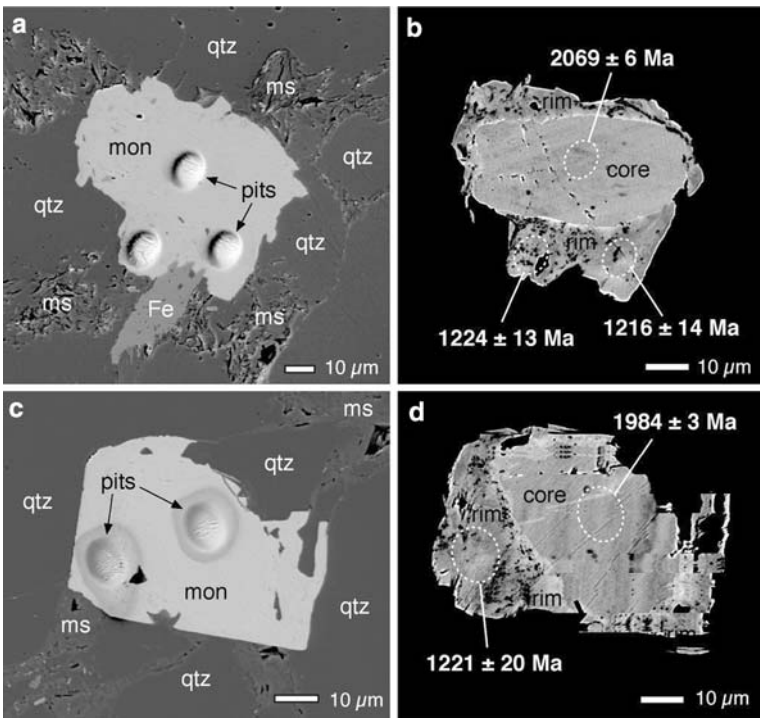

Fig.12 **a** BSE image of monazite crystal with three SHRIMP pits. **b** High-contrast BSE image of monazite in **a**, showing a rounded core with an incomplete, inclusion-rich rim. The oval outlines correspond with analytical pits (monazite core is a $^{207}Pb/^{206}Pb$ date whereas monazite overgrowths are $^{208}Pb/^{232}Th$ dates). Barnett Peak, UWA 114338. **c** BSE image of coarse monazite crystal with two SHRIMP pits. **d** High-contrast BSE image of monazite in **c**, showing an inclusion-rich rim surrounding a compositionally distinct core. Barnett Peak, UWA 114325. The oval outlines correspond with analytical pits (monazite core is a $^{207}Pb/^{206}Pb$ date whereas monazite rim is a $^{208}Pb/^{232}Th$ date). SHRIMP data from Rasmussen et al. (2002)

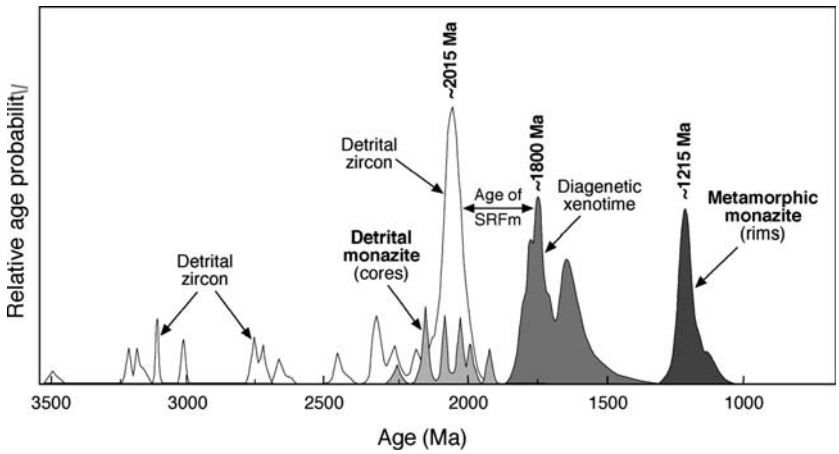

Fig. 13 Probability plot showing age data from detrital zircon and monazite, diagenetic xenotime and metamorphic monazite from the Stirling Range Formation (SHRIMP data from Rasmussen et al. 2002, 2004)

La than either the detrital core or the outer part of the rim. The middle REE (Pr–Gd) display an inverse relationship with La, and are enriched compared to the core and outer rim. The outer, broader part of the rim contains significantly more La, which rises slightly toward the crystal margin, indicating a pattern of La enrichment during monazite growth. In contrast, the Sm (and MREE) content decreases sharply in the outer zone, and then displays a gradual depletion toward the outer margin. The reason for this is not known, but it is a consistent pattern that was observed in every monazite crystal ($n = 10$) that was mapped by WDS. A similar pattern was observed in inclusion-rich metamorphic monazite crystals in prehnite–pumpellyite facies shales of the Soanesville greenstone belt in the central Pilbara Craton (Rasmussen et al. 2007), and in low-temperature monazite nodules from Wales (Read et al. 1987; Milodowski and Zalasiewicz 1991).

Some of the thorium released by the dissolution of the high-Th detrital cores combined with SiO_2 and precipitated in the overgrowths as discrete crystals of $ThSiO_4$ (see equation). Overall, the metamorphic monazite incorporated less Ca, Y, Th and U than was present in the high-temperature precursor, possibly reflecting the inability of low-temperature monazite to incorporate substantial amounts of these elements into its structure relative to igneous and high-grade metamorphic varieties. Again, the relatively low Ca, Y, Th and U contents, elevated Eu values and lack of a Ce anomaly in the monazite overgrowths have been

observed in monazite from low-grade metamorphic rocks elsewhere (Rosenblum and Mosier 1983; Read et al. 1987; Burnotte et al. 1989; Milodowski and Zalasiewicz 1991; Cabella et al. 2001; Rasmussen et al. 2007).

$$\underset{\text{detrital monazite}}{(\text{La,Ce,Nd,Th})\text{PO}_4} + \underset{\text{quartz}}{\text{SiO}_2} + \underset{\text{fluid}}{\text{Eu}^{3+}} \rightarrow \underset{\text{low-grade monazite}}{(\text{La,Ce,Nd})\text{PO}_4} + \text{ThSiO}_4 + \underset{\text{fluid}}{\text{Ca}^{2+}}$$

Ion microprobe U–Pb and Th–Pb data and electron microprobe analyses (Table 1) obtained from the overgrowths suggest that radiogenic Pb from the detrital cores was not reincorporated into the newly grown monazite, consistent with observations elsewhere that monazite typically excludes Pb during its growth.

Stability of monazite during low-grade metamorphism

Numerous mineral reactions have been inferred for the formation and destruction of monazite during metamorphism (e.g. Catlos et al. 2002; Kohn and Malloy 2004), reflecting the complex behaviour of monazite under different *P–T–X* conditions. During retrograde metamorphism, monazite has been linked to many alteration products, including allanite, apatite, epidote, rhabdophane and low-temperature monazite (Lanzirotti and Hanson 1996; Finger et al. 1998; Townsend et al. 2000). During prograde metamorphism, monazite shows a marked increase in abundance at the expense of allanite at lower amphibolite-facies conditions (Smith and Barreiro 1990; Catlos et al. 2002). However, monazite may also be stable in metapelitic rocks at much lower temperatures, and detailed textural studies have provided compelling evidence for the growth of monazite during prehnite–pumpellyite facies metamorphism (e.g. Rasmussen et al. 2005).

There have been surprisingly few studies addressing the stability and behaviour of monazite during low-grade metamorphism. Although detrital monazite has been reported as a component of greenschist facies rocks, it is generally considered to be unstable and to disappear by the onset of, or during, amphibolite facies metamorphism (Overstreet 1967; Smith and Barreiro 1990). However, some studies have suggested that detrital monazite may survive mid-amphibolite facies (Williams 2001), and even granulite facies metamorphism (Suzuki et al. 1994; Rubatto et al. 2001). A major limitation to our understanding of the behaviour of detrital monazite during prograde metamorphism has been the lack of textural evidence for the mineral reactions leading to its destruction. Our study shows that detrital Th-rich monazite is unstable during low-grade metamorphism, and undergoes replacement via dissolution and reprecipitation, forming low-Th monazite overgrowths with trace amounts of $ThSiO_4$ inclusions.

The preservation potential of composite monazite crystals at higher metamorphic grades may be assessed from the results of a recent study. Wing et al. (2003) identified similar composite grains in metapelites with moderate to high Ca contents, in which monazite disappeared at the biotite isograd (400–500°C), coinciding with the first appearance of allanite porphyroblasts. In rocks with low-Ca bulk compositions, composite monazite grains were preserved until the onset of amphibolite facies metamorphism (Wing et al. 2003). The preservation of composite monazite throughout greenschist facies, and possibly into amphibolite facies, metamorphism is likely to have important implications for geochronological studies using monazite.

Implications for monazite geochronology

Accessory minerals such as monazite have become important tools in establishing the timing and duration of medium- and high-grade metamorphism. A goal of metamorphic geology is to link the growth of accessory minerals to key chemical reactions such as the appearance of major metamorphic silicate minerals, including staurolite (Smith and Barreiro 1990; Kingsbury et al. 1993; Kohn and Malloy 2004) and kyanite (Ferry 2000; Wing et al. 2003). Such an approach can provide high-precision dates for reactions that can be used to calculate metamorphic pressures and temperatures, and hence define points on *P–T–t* paths. In low-grade metamorphic rocks it is difficult to link the growth of accessory minerals to the development of diagnostic metamorphic minerals because conspicuous mineral growth is commonly lacking. This is the case in the Stirling Range Formation; however, the textural relationships between the monazite rims and the deformational fabric clearly indicate that monazite growth was synchronous with fabric development and peak metamorphism. Hence, monazite can be used to date peak metamorphism and syntectonic cleavage formation.

However, because most monazite crystals comprise a detrital core and metamorphic rim, attempts to date metamorphism using whole-grain techniques are likely to give erroneous results. Indeed, in situ microbeam methods (e.g. SIMS, LA–ICP–MS) may also give confusing data due to overlap of the ion beam or laser spot onto detrital cores and metamorphic rims. In the case of the Stirling Range Formation, it may be expected that dates spanning more than one billion years (from 2.2 to 1.2 Ga) could be obtained depending on beam placement. These observations may help to explain the presence of discordant monazite in some metamorphic rocks elsewhere (e.g. Parrish 1990). Our results emphasize the importance of an integrated

approach using a combination of BSE imaging, X-ray mapping and electron microprobe analysis (e.g. Townsend et al. 2000; Kohn et al. 2005; Rasmussen et al. 2007) to distinguish between detrital and metamorphic monazite and/or mixtures of the two.

Conclusions

Monazite is abundant as idioblastic and xenoblastic crystals in low-grade metasedimentary rocks from the Stirling Range Formation in southwestern Australia. Back-scattered electron imaging and X-ray element mapping of the monazite reveal the presence of compositionally distinct cores surrounded by inclusion-rich rims. The ages of the cores (2.2–1.9 Ga) overlap with dates from detrital zircon grains (3.5–2.0 Ga) in the succession, demonstrating a detrital origin for the cores. Many of the cores have scalloped and embayed margins, providing textural evidence for the partial to near-complete dissolution of the former detrital grains.

The monazite rims are characterised by lower Ca, Y, Th, U and Pb, and higher Eu, contents than the detrital cores, and by a pronounced zonation of the light and middle REE. Thorium silicate inclusions in the monazite rims suggest that dissolution of the Th-rich cores and growth of the Th-poor rims were closely linked in time, and that both were related to low-grade metamorphism. Textural relationships between the monazite overgrowths (~1.2 Ga) and deformational fabric show that monazite growth was synchronous with deformation and peak metamorphism in the Stirling Range Formation.

Our results clearly show that high-Th detrital monazite is unstable during low-grade regional metamorphism and undergoes dissolution and reprecipitation, resulting in the growth of low-Th metamorphic monazite and discrete crystals of $ThSiO_4$. Dissolution of detrital monazite grains appears to have been the main source of REE and P for new monazite growth. This reaction is likely to operate in low-grade metasedimentary rocks with low-Ca bulk compositions, where it acts to destroy detrital monazite during prograde metamorphism. In cases where the dissolution of detrital monazite is incomplete, monazite with the appearance of purely metamorphic forms (e.g. idioblastic or xenoblastic), may actually comprise multiple age domains. Attempts to date such composite crystals, without prior chemical and textural characterisation, are likely to be flawed.

Acknowledgments We thank Ian Fletcher and Bryan Krapez for comments and discussion, and the staff of CMCA at UWA for their assistance. SEM imaging and microanalysis were carried out using facilities at the CMCA (UWA), which is supported by funding from the University, and the Western Australian and Australian Governments. Samples were collected with the permission of the Western Australian Department of Conservation and Land Management. The paper was improved by comments from Gerhard Franz and an anonymous reviewer.

References

Beeson J (1991) A field and experimental study of the structure of the Albany Mobile Belt, Western Australia. Ph.D thesis, The University of Western Australia

Beeson J, Delor CP, Harris LB (1988) A structural and metamorphic traverse across the Albany Mobile Belt, Western Australia. Precambrian Res 40/41:117–136

Bengtson S, Rasmussen B, Krapez B (2007) The Paleoproterozoic megascopic Stirling biota. Paleobiology, vol 33 (in press)

Black LP, Harris LB, Delor CP (1992) Reworking of Archaean and Early Proterozoic components during a progressive, Middle Proterozoic tectonothermal event in the Albany Mobile Belt, Western Australia. Precambrian Res 59:95–123

Bodorkos S, Clark DJ (2004) Evolution of a crustal-scale transpressive shear zone in the Albany-Fraser Orogen, SW Australia: 2. Tectonic history of the Coramup Gneiss and a kinematic framework for Mesoproterozoic collision of the West Australian and Mawson cratons. J Metamorp Geol 22:713–731

Boulter CA (1979) On the production of two inclined cleavages during a single folding event; Stirling Range, S.W. Australia. J Struct Geol 1:207–219

Burnotte E, Pirard E, Michel G (1989) Genesis of gray monazites: evidence from the Paleozoic of Belgium. Econ Geol 84:1417–1429

Cabella R, Lucchetti G, Marescotti P (2001) Authigenic monazite and xenotime from pelitic metacherts in pumpellyite–actinolite-facies conditions, Sestri-Voltaggio Zone, central Liguria, Italy. Can Mineral 39:717–727

Catlos EJ, Gilley LD, Harrison TM (2002) Interpretation of monazite ages obtained via in situ analysis. Chem Geol 188:193–215

Chang LLY, Howie RA, Zussman J (1996) Rock-forming minerals. Non-silicates. vol 5B. Longman, London

Cherniak DJ, Watson EB, Grove M, Harrison TM (2004) Pb diffusion in monazite: a combined RBS/SIMS study. Geochim Cosmochim Acta 68:829–840

Clark DJ, Kinny PD, Post NJ, Hensen BJ (1999) Relationships between magmatism, metamorphism and deformation in the Fraser Complex, Western Australia: constraints from new SHRIMP U–Pb zircon geochronology. Aust J Earth Sci 46:923–932

Clark DJ, Hensen BJ, Kinny PD (2000) Geochronological constraints for a two-stage history of the Albany-Fraser Orogen, Western Australia. Precambrian Res 102:155–183

Condie KC, Myers JS (1999) Mesoproterozoic Fraser complex: geochemical evidence for multiple subduction related sources of lower crustal rocks in the Albany-Fraser Orogen, Western Australia. Aust J Earth Sci 46:875–882

Cruse T (1991) The sedimentology, depositional environment and Ediacaran fauna of Mondurup and Barnett Peaks, Stirling Range Formation, Western Australia. B.Sc (Hons) thesis, The University of Western Australia

Cruse T, Harris LB (1994) Ediacaran fossils from the Stirling Range Formation, Western Australia. Precambrian Res 67:1–10

Cruse T, Harris LB, Rasmussen B (1993) The discovery of Ediacaran trace and body fossils in the Stirling Range Formation, Western Australia: implications for sedimentation and deformation during the ''Pan-African'' orogenic cycle. Aust J Earth Sci 40:292–296

Dawson GC, Krapez B, Fletcher IR, McNaughton NJ, Rasmussen B (2003) 1.2 Ga thermal metamorphism in the Albany-Fraser Orogen of Western Australia: consequence of collision or regional heating by dyke swarms? J Geol Soc Lond 160:29–37

DeWolf CP, Belshaw N, O'Nions RK (1993) A metamorphic history from micron-scale $^{207}Pb/^{206}Pb$ chronometry of Archean monazite. Earth Planet Sci Lett 120:207–220

Donnot M, Guigues J, Lulzac Y, Magnien A, Parfenoff A, Picot P (1973) Un nouveau type de gisement d'europium: la monazite grise à europium en nodules dans les schistes paléozoïques de Bretagne. Mineral Dep 8:7–18

Ferry JM (2000) Patterns of mineral occurrence in metamorphic rocks. Am Mineral 85:1573–1588

Finger F, Broska I, Roberts MP, Schermaier A (1998) Replacement of primary monazite by apatite–allanite–epidote coronas in an amphibolite facies granite gneiss from the eastern Alps. Am Mineral 83:248–258

Franz G, Andrehs G, Rhede D (1996) Crystal chemistry of monazite and xenotime from Saxothuringian–Moldanubian metapelites, NE Bavaria, Germany. Eur J Mineral 8:1097–1108

Gardés E, Jaoul O, Montel J-M, Seydoux-Guillaume A-M, Wirth R (2006) Pb diffusion in monazite: an experimental study of $Pb^{2+} + Th^{4+} \Leftrightarrow 2Nd^{3+}$ interdiffusion. Geochim Cosmochim Acta 70:2325–2336

Gibson HD, Carr SD, Brown RL, Hamilton MA (2004) Correlations between chemical and age domains in monazite, and metamorphic reactions involving major pelitic phases: an integration of ID-TIMS and SHRIMP geochronology with Y–Th–U X-ray mapping. Chem Geol 211:237–260

Harris LB, Beeson J (1993) Gondwanaland significance of Lower Palaeozoic deformation in central India and SW Western Australia. J Geol Soc London 150:811–814

Kingsbury JA, Miller CF, Wooden JL, Harrison TM (1993) Monazite paragenesis and U–Pb systematics in rocks of the eastern Mojave Desert, California, U.S.A.: implications for thermochronometry. Chem Geol 110:147–167

Kohn MJ, Malloy MA (2004) Formation of monazite via prograde metamorphic reactions among common silicates: implications for age determinations. Geochim Cosmochim Acta 68:101–113

Kohn MJ, Wieland MS, Parkinson CD, Upreti BN (2005) Five generations of monazite in Langtang gneisses: implications for chronology of the Himalayan metamorphic core. J Metamorp Geol 23:399–406

Lanzirotti A, Hanson GN (1996) Geochronology and geochemistry of multiple generations of monazite from the Wepawaug Schist, Connecticut, U.S.A.: implications for monazite stability in metamorphic rocks. Contrib Mineral Petrol 125:332–340

Lev SM, McLennan SM, Meyers WJ, Hanson GN (1998) A petrographic approach for evaluating trace-element mobility in a black shale. J Sed Res 68:970–980

McDonough WF, Sun S-s (1995) The composition of the Earth. Chem Geol 120:223–253

Milodowski AE, Zalasiewicz JA (1991) Redistribution of rare earth elements during diagenesis of turbidite/hemipelagite mudrock sequences of Llandovery age from Central Wales. In: Morton AC, Todd SP, Haughton PDW (eds) Developments in sedimentary provenance studies. Geological Society Special Publication 57, pp 101–124

Muhling PC, Brakel AT (1985) Mount Barker-Albany 1:250000 geological series—explanatory notes. Geological Survey of Western Australia, Perth

Nelson DR, Myers JS, Nutman AP (1995) Chronology and evolution of the middle Proterozoic Albany-Fraser orogen, Western Australia. Aust J Earth Sci 42:481–495

Overstreet WC (1967) The geological occurrence of monazite. US Geol Surv Prof Paper 530:1–327

Parrish RR (1990) U–Pb dating of monazite and its application to geological problems. Can J Earth Sci 27:1431–1450

Rasmussen B, Fletcher IR (2004) Zirconolite: a new U–Pb chronometer for mafic igneous rocks. Geology 32:785–788

Rasmussen B, Fletcher IR, McNaughton NJ (2001) Dating low-grade metamorphic events by SHRIMP U–Pb analysis of monazite in shales. Geology 29:963–966

Rasmussen B, Bengtson S, Fletcher IR, McNaughton NJ (2002) Discoidal impressions and trace-like fossils more than 1200 million years old. Science 296:1112–1115

Rasmussen B, Fletcher IR, Bengtson S, McNaughton NJ (2004) SHRIMP U–Pb dating of diagenetic xenotime in the Stirling Range Formation, Western Australia: 1.8 billion year minimum age for the Stirling biota. Precambrian Res 133:329–337

Rasmussen B, Fletcher IR, Sheppard S (2005) Isotopic dating of the migration of a low-grade metamorphic front during orogenesis. Geology 33:773–776

Rasmussen B, Sheppard S, Fletcher IR (2006a) Testing ore deposit models using in situ U–Pb geochronology of hydrothermal monazite: Paleoproterozoic gold mineralization in northern Australia. Geology 34:77–80

Rasmussen B, Muhling JR, Fletcher IR, Wingate MTD (2006b) In situ SHRIMP U–Pb dating of monazite integrated with petrology and textures: does bulk composition control whether monazite forms in low-Ca pelitic rocks during amphibolite facies metamorphism? Geochim Cosmochim Acta 70:3040–3058

Rasmussen B, Fletcher IR, Muhling JR (2007) In situ U–Pb dating and element mapping of three generations of monazite: unravelling cryptic tectonothermal events in low-grade terranes. Geochim Cosmochim Acta 71:670–690

Read D, Cooper DC, McArthur JM (1987) The composition and distribution of nodular monazite in the Lower Palaeozoic rocks of Great Britain. Mineral Mag 51:271–280

Rosenblum S, Mosier EL (1983) Mineralogy and occurrence of europium-rich dark monazite. US Geol Surv Prof Paper 1181, pp 1–67

Rubatto D, Williams IS, Buick IS (2001) Zircon and monazite response to prograde metamorphism in the Reynolds Range, central Australia. Contrib Mineral Petrol 140:458–468

Seydoux-Guillaume A-M, Paquette J-L, Wiedenbeck M, Montel J-M, Heinrich W (2002) Experimental resetting of the U–Th–Pb systems in monazite. Chem Geol 191:165–181

Smith HA, Barreiro B (1990) Monazite U–Pb dating of staurolite grade metamorphism in pelitic schists. Contrib Mineral Petrol 105:602–615

Spear FS, Pyle JM (2002) Apatite, monazite, and xenotime in metamorphic rocks. In: Kohn MJ, Rakovan J, Hughes JM (eds) Phosphates: geochemical, geobiological and materials importance. Reviews in mineralogy and geochemistry, vol 48. Mineralogical Society of America, Washington DC, pp 293–335

Stern RA, Berman RG (2000) Monazite U–Pb and Th–Pb geochronology by ion microprobe, with an application to in situ dating of an Archean metasedimentary rock. Chem Geol 172:113–130

Suzuki K, Adachi M, Kajizuka I (1994) Electron microprobe observations of Pb diffusion in metamorphosed detrital monazites. Earth Planet Sci Lett 128:391–405

Teufel S, Heinrich W (1997) Partial resetting of the U–Pb isotope system in monazite through hydrothermal experiments: an SEM and U–Pb isotope study. Chem Geol 137:273–281

Townsend KJ, Miller CF, D'Andrea JL, Ayers JC, Harrison TM, Coath CD (2000) Low temperature replacement of monazite in the Ireteba granite, Southern Nevada: geochronological implications. Chem Geol 172:95–112

Williams CT (1996) Analysis of rare earth minerals. In: Jones AP, Wall F, Williams CT (eds) Rare earth minerals: chemistry, origin and ore deposits. Chapman and Hall, London, pp 327–348

Williams IS (2001) Response of detrital zircon and monazite, and their U–Pb isotopic systems, to regional metamorphism and host-rock partial melting, Cooma Complex, southeastern Australia. Aust J Earth Sci 48:557–580

Wing BA, Ferry JM, Harrison TM (2003) Prograde destruction and formation of monazite and allanite during contact and regional metamorphism of pelites: petrology and geochronology. Contrib Mineral Petrol 145:228–250

Wingate MTD, Campbell IH, Harris LB (2000) SHRIMP baddeleyite age for the Fraser dyke swarm, southeast Yilgarn Craton, Western Australia. Aust J Earth Sci 47:309–313